



Enhanced electrochemical properties of ZnO encapsulated in carbon nanofibers as anode material for lithium-ion batteries

Yuhao Li¹ · Mingyu Zhang¹ · Qizhong Huang¹ · Peng Zhou¹ · Ping Xu¹ · Zhenghao Guo¹ · Kaibin Dai¹

Received: 23 April 2020 / Revised: 1 May 2020 / Accepted: 6 May 2020 / Published online: 16 May 2020
© Springer-Verlag GmbH Germany, part of Springer Nature 2020

Abstract

The amorphous ZnO particles encapsulated in porous nitrogen-doped carbon nanofibers (ZnO@PN-CNFs) are synthesized by electrospinning process and heat treatment. The enhanced electrochemical properties of ZnO@PN-CNFs are based on the porous nanostructure, high length/diameter (L/D) ratio, doped nitrogen, and uniform distributed amorphous ZnO nanoparticles. The results show amorphous ZnO particles in carbon nanofibers avoid the pulverization and alleviated the volume expansion, as well as make the cycling of the anode quickly reach stable. Furthermore, the nitrogen-doped carbon improves electron conductivity while one-dimensional (1D) nanofibers with high L/D ratio own a short diffusion path and high electronic transportation efficiency along the longitudinal direction. Meanwhile, the porous nanostructure from urea pyrolysis produces thinner wall and further shortens the ionic transport distance. Therefore, high capacity and long-cycling life are achieved. And the ZnO@PN-CNF electrode shows a high discharge capacity (1073.2 mAh g⁻¹ at 0.1 A⁻¹) after 100 cycles. Moreover, the ZnO@PN-CNF electrode presents a high discharge capacity of 703.1 mAh g⁻¹ even at 1 A⁻¹ after 400 cycles. In this work, urea not only stops the ZnO from crystallization, leading to uniform distributed amorphous small ZnO particles, but also makes numerous pores in the carbon nanofibers, enlarging the touching area with electrolyte and shortening the transport distance to ZnO particles. It is a promising way by adding urea to alleviate volume expansion and pulverization of the crystal particles and then enhance the performance of electrode.

Keywords Zinc oxide · Amorphous · Electrospinning · Anode · Lithium-ion batteries

Introduction

Lithium-ion batteries (LIBs) already widely used in consumer electronic equipment and grid-scale storage systems. Aiming to the desired energy storage, high power density and energy density are eager to be developed for high-performance LIBs [1–5]. However, the commercial graphite anode has a low theoretical capacity (372 mAh g⁻¹), which places restrictions on the application of LIBs [6–8]. Transition metal oxides (TMOs, M = Mn, Zn, Cr, Ni, etc.) are attractive because of

their high reversible capacities [9–15]. Among these, ZnO is supposed to be a promising candidate of anode materials for LIBs on account of its large theoretical capacity of 978 mAh g⁻¹. However, the pulverization issue caused by the severe volume changes (228%) of crystal ZnO in LIBs hindered its practical application, resulting in a loss of electric contact, rapid capacity fading during cyclic process, and poor rate performance [16–19].

Many strategies have been applied to suppress the effect of crystal ZnO pulverization, such as morphological design of nanostructures [20, 21], hybridizing with other materials [6, 17, 18], and introduction of carbon materials [7, 16, 19, 22]. And one of the most effective strategies is to reduce ZnO size, which could decrease the mechanical stress produced by redox reaction with Li-ions, and thus restrained the inclination to fracture and crack [23, 24]. The one-dimensional (1D) nanostructure can shorten the lengths of Li-ion transport path to provide a superior rate capability [25, 26]. Furthermore, the presence of carbon could improve conductivity and mitigate volume changes so as to improve long-cycle stability [27–29]. Therefore, 1D nanostructure carbon compounded with ZnO

Electronic supplementary material The online version of this article (<https://doi.org/10.1007/s11581-020-03610-9>) contains supplementary material, which is available to authorized users.

✉ Mingyu Zhang
zhangmingyu@csu.edu.cn

¹ National Key Laboratory of Science and Technology for National Defence on High-Strength Structural Materials, Powder Metallurgy Research Institute, Central South University, Changsha 410083, People's Republic of China

had been widely studied because the nanostructure provides conductive network and transmission channels, which is beneficial to improve electrochemical performance [23, 30]. Electrospinning is an efficient way to prepare 1D nanostructure [12, 31, 32]. For instance, Zhao et al. prepared the ZnO/carbon nanofibers composited by petroleum asphalt-derived carbon. The composite anode possessed a reversible capacity of 702 mAh g⁻¹ at 0.2 A⁻¹ after 200 cycles [30]. Despite these achievements, the ZnO size in carbon is not small enough to avoid the pulverization. With the decrease of the particle size, the crystal ZnO particles are gradually transformed into amorphous particles.

Amorphization is considered to be advantageous to improve electrochemical performance. For crystal materials, the change from crystal state to amorphous state is electrochemically driven during the process of lithium ion insertion [33, 34]. In addition, the contact between crystals becomes worse, and then the conductive property becomes worse, resulting in a bad reaction performance with lithium ions. For amorphous materials, the volume expansion is effectively alleviated. Therefore, minimizing the pulverization process could stabilize the cycling faster [35–37]. Moreover, amorphous materials have superior performance during discharge/charge processes because of active sites on their surface [26, 36]. Therefore, it is an efficacious pathway to enhance electrochemical properties by improving amorphous level of ZnO particles.

Herein, we proposed an approach to make the electrospinning of nitrogen-doped carbon nanofibers generate both mesopores in carbon nanofibers and uniform distributed amorphous ZnO particles by introducing urea as pore former. The porous nitrogen-doped carbon nanofibers encapsulated ZnO (ZnO@PN-CNFs) were successfully prepared by electrospinning process and heat treatment. It was demonstrated that the amorphous ZnO particles that disperse uniformly in the porous carbon nanofibers could obtain a high discharge capacity of 1073.2 mAh g⁻¹ after 100 cycles at 0.1 A⁻¹. And the ZnO@PN-CNF electrode showed an excellent rate performance and high specific capacity compared with crystallite ZnO encapsulated in carbon nanofibers (ZnO@N-CNFs).

Experimental section

Preparation of the ZnO@PN-CNFs

First, 0.45 g polyacrylonitrile (PAN, AR, M_w 150 000, Sigma-Aldrich) was dissolved into 3 mL N, N-dimethylformamide (DMF, AR, Sinopharm), subsequently stirred (at 60 °C) for 1 h to form solution A. A total of 0.4 g zinc acetate dihydrate (Zn(CH₃COO)₂·2H₂O, AR, Sinopharm) and 0.07 g urea (AR, Sinopharm) were dissolved into 3 mL DMF and upon 1 h stirring to get solution B. Next, solution B was gradually

added to solution A, stirred for 24 h at 25 °C to form a uniform solution and then it was transferred into a plastic injector. During electrospinning, the distance between the aluminum collector and the injector needle was 20 cm. A positive voltage of 10–12 kV was conducted between the aluminum collector and the injector needle. The obtained precursor nanofibers were dried at 60 °C for 12 h and subsequently stabilized at 220 °C in air for 3 h. After cooling to room temperature, the precursor nanofibers were calcinated at 650 °C in Ar for 2 h. And finally, the ZnO@PN-CNFs were synthesized. For comparison, the same procedures were applied to synthesize ZnO@N-CNFs without urea.

Material characterization

X-ray diffraction (XRD, Rigaku Dmax/2550VB+18KW) was used to characterize the crystal structure of the samples. The morphology of the samples was observed by scanning electron microscopy (SEM, FEI Nova Nano SEM230) and transmission electron microscopy (TEM, JEOL JEM-2010). X-ray photoelectron spectroscopy (XPS, Thermo ESCALAB 250XI) was employed with Al K α (h ν = 1486.8 eV) as the excitation source. The Quadrasorb SI surface characterization analyzer with nitrogen adsorption-desorption isotherms was used for evaluating the specific surface areas of samples as well as pore size distribution. The thermogravimetric analysis of ZnO@PN-CNFs was conducted with a Netzsch STA 409EP TGA-DSC apparatus. The Raman spectrum was obtained by using a Raman spectrometer (Horiba, LabRAM Aramis).

Electrochemical measurements

To obtain the electrodes, mix prepared nanofibers, acetylene carbon black, and polyvinylidene fluoride at mass ratios of 7:2:1, dissolved in N-methyl-2-pyrrolidinone to form slurry. After that, the slurry was casted onto Cu foil and dried at 60 °C overnight under vacuum then cut into circular pieces. The loading active material density on Cu foil was 0.8–1.0 mg cm⁻². Thereafter, the CR2032 coin-type half-cells were assembled in an argon-filled glove box with polypropylene film (Celgard 2400) as separator, Li metal as the reference electrode, and LiPF₆ (1M, EC: DMC = 1:1) as electrolyte. The electrode capability was measured by a battery testing system (LANDCT2001A) within a voltage area of 0.005–3.0 V. The electrochemical workstation (CHI760E) was employed on the tests of cyclic voltammetry (CV) within 0.005–3.0 V and the EIS measurements with the frequency range of 100 kHz to 0.01 Hz.

Results and discussion

The fabrication process of ZnO@PN-CNFs is illustrated in Fig. 1. The samples were divided to two groups: one was

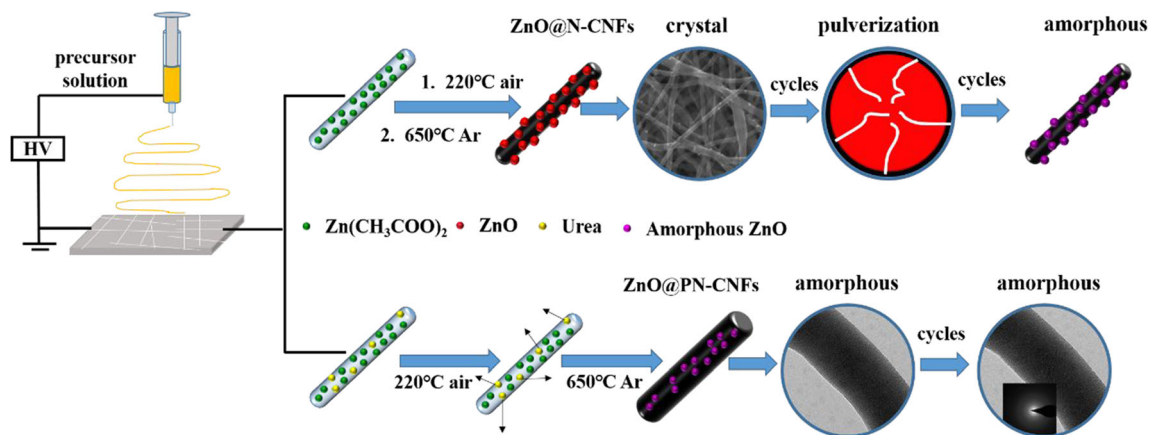


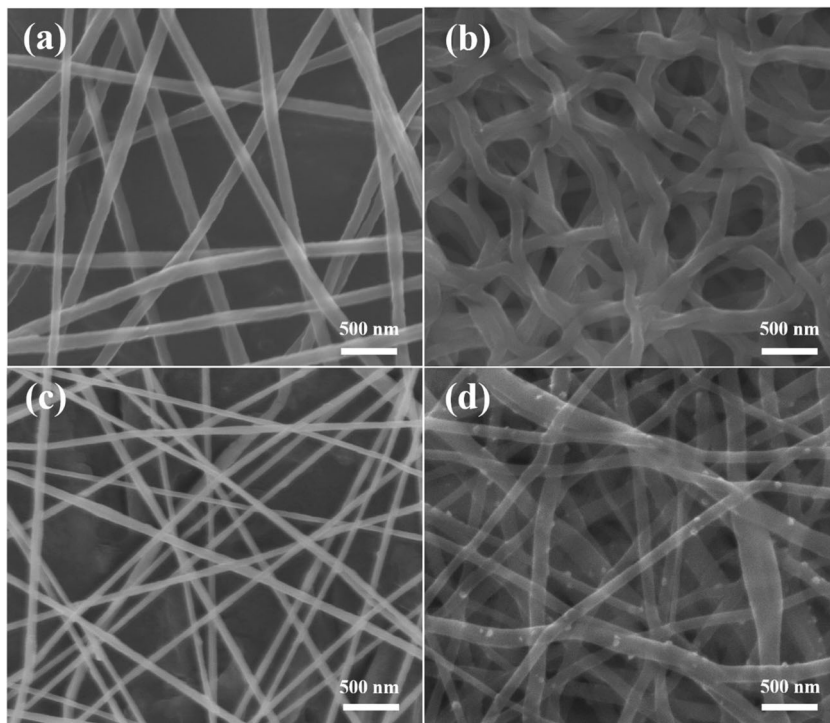
Fig. 1 Schematic illustration of the synthesis process and changes during cycling of ZnO@PN-CNFs and ZnO@N-CNFs

ZnO@N-CNFs as the contrast samples and the other was ZnO@PN-CNFs with urea addition in the precursor solution. The electrospinning precursor nanofibers were transformed into ZnO@N-CNFs and ZnO@PN-CNFs after the subsequent stabilization and carbonization. It was believed that the presence of carbon can alleviate the volume change of zinc oxide during Li^+ insertion and extraction processes [38]. Although compounded with carbon, crystalline ZnO in ZnO@N-CNFs will pulverize after repeated Li^+ insertion and extraction, and then the crystal state was transformed into an amorphous state. However, amorphous ZnO in ZnO@PN-CNFs could still maintain amorphous state even after many cycles.

The PAN-derived nitrogen-doped carbon fibers could improve the electron conductivity, provide ion transport

channels, and shorten the ion diffusion path during lithiation/delithiation processes [39, 40]. Figure 2 a and b show the SEM images of the ZnO@PN-CNFs precursor and ZnO@PN-CNFs, respectively. The precursor nanofibers had uniform nanostructure with smooth surface. However, the addition of urea significantly enlarged the diameters of the ZnO@PN-CNF precursor. After stabilization and carbonization, the ZnO@PN-CNFs became a twisted and crooked structure like noodles without crystalline ZnO on the surface in Fig. 2b. And Fig. 2 c and d show the SEM images of the ZnO@N-CNF precursor and ZnO@N-CNFs, respectively. As the contrast sample, many crystalline ZnO particles were mounted on the surface of the ZnO@N-CNFs, as revealed in Fig. 2d. The average diameter of the ZnO@PN-CNFs was

Fig. 2 SEM image of **a** ZnO@PN-CNFs precursor, **b** ZnO@PN-CNFs, **c** ZnO@N-CNFs precursor, **d** ZnO@N-CNFs



about 130 nm while that of ZnO@N-CNFs is about 100 nm. The thicker diameters of ZnO@PN-CNFs are attributed to the effect of urea pore former.

To further investigate the microstructure of ZnO@PN-CNFs, TEM was employed. As shown in Fig. 3, ZnO crystallite was observed neither on the nanofibers surface nor inside the nanofibers. The crystal lattice fringe of ZnO was not found in Fig. 3b of the high-resolution TEM (HRTEM) images of ZnO@PN-CNFs either, which indicates the amorphous state of ZnO. Amorphous ZnO helps to achieve higher insertion and extraction rates of Li ions and accelerates to equilibrium as soon as possible without the pulverization of the ZnO in the oxidation reduction reactions (ORR), which simultaneously improves the electrical conductivity, cycling stability, and interfacial contact property [25, 36]. Thereafter, element mapping identified the elemental distribution of ZnO@PN-CNFs. Figure 3 c–f present elemental mapping results revealing the distribution of C, Zn, O, and N elements. The images of Zn and O elements indicated that ZnO was homogeneously distributed in the nanofibers, which was conducive to avoid the pulverization and alleviate the volume expansion. The presence of C and N indicated the formation of nitrogen-doped carbon from carbonized PAN, which was confirmative to enhance the conductivity as well as provide many active sites [23, 41]. The TEM and HRTEM of ZnO@N-CNFs are shown in Fig. S1.

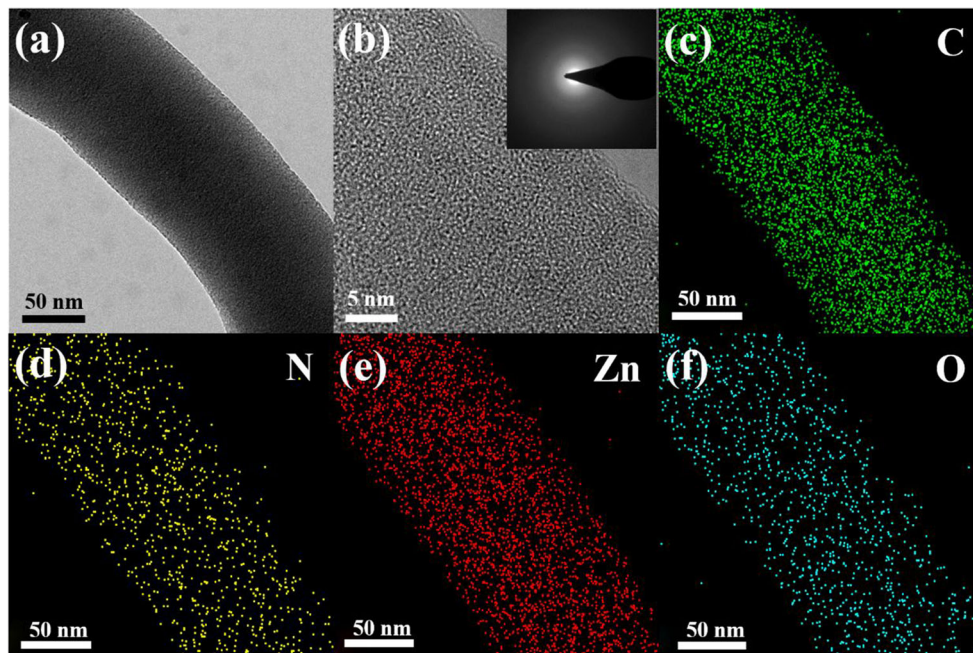
The composition and crystallographic structure of ZnO@PN-CNFs had been further investigated. Figure 4 a shows the XRD patterns of ZnO@PN-CNFs and ZnO@CNFs, respectively. For the XRD patterns of ZnO@N-CNFs, all the characteristic peaks of ZnO@N-CNFs can be well corresponding to ZnO (JCPDS 36-1451)

[42]. The XRD patterns of both materials showed a broad diffraction peak at about 23° , attributed to the (002) lattice planes of carbon [23]. The XRD patterns of ZnO@PN-CNFs only showed a broad diffraction peak at 23° , and no obvious peaks related to ZnO were detected while that of ZnO@N-CNFs indicated the ZnO was well crystallized corresponding to the SEM image of Fig. 2d. This can be attributed to the coexistence of urea (as a porogen) and zinc acetate suppressing the crystallization of ZnO, forming an amorphous state or transforming into smaller nanosized particles [23, 43]. The XRD result also confirmed the amorphous state of ZnO in ZnO@PN-CNFs, which was consistent with TEM observation.

To determine the content of ZnO in ZnO@PN-CNFs, TGA analysis was conducted from 25 to 1000 °C in air (Fig. 4b). The slight weight loss occurred in 25–200 °C, which is corresponding to evaporation of absorbed water. And an apparent weight loss occurred in 200–900 °C due to the combustion of carbon. The calculated ZnO content of ZnO@PN-CNFs from the TGA data was 35.54 wt%.

The BET-specific surface area and related pore-size distribution were studied by N_2 adsorption-desorption isotherms (Fig. 4c, d). The BET-specific surface area of the ZnO@PN-CNFs and ZnO@N-CNFs is $30.72 \text{ m}^2 \text{ g}^{-1}$ and $29.28 \text{ m}^2 \text{ g}^{-1}$, respectively. Both isotherms display noticeable uptake at a relative pressure of $P/P_0 < 0.01$, revealing the existence of microporous structure [44]. The hysteresis loop of isotherms suggested the existence of mesopores [39, 44]. The pore size distribution was obtained by DFT method, as displayed in Fig. 4 c and d. Compared to ZnO@N-CNFs, the specific surface area of ZnO@PN-CNFs was not significantly improved, which occurred because urea plays a role during the

Fig. 3 a TEM image of ZnO@PN-CNFs. b HRTEM image of ZnO@PN-CNFs. c–f Corresponding elemental mapping images of ZnO@PN-CNFs



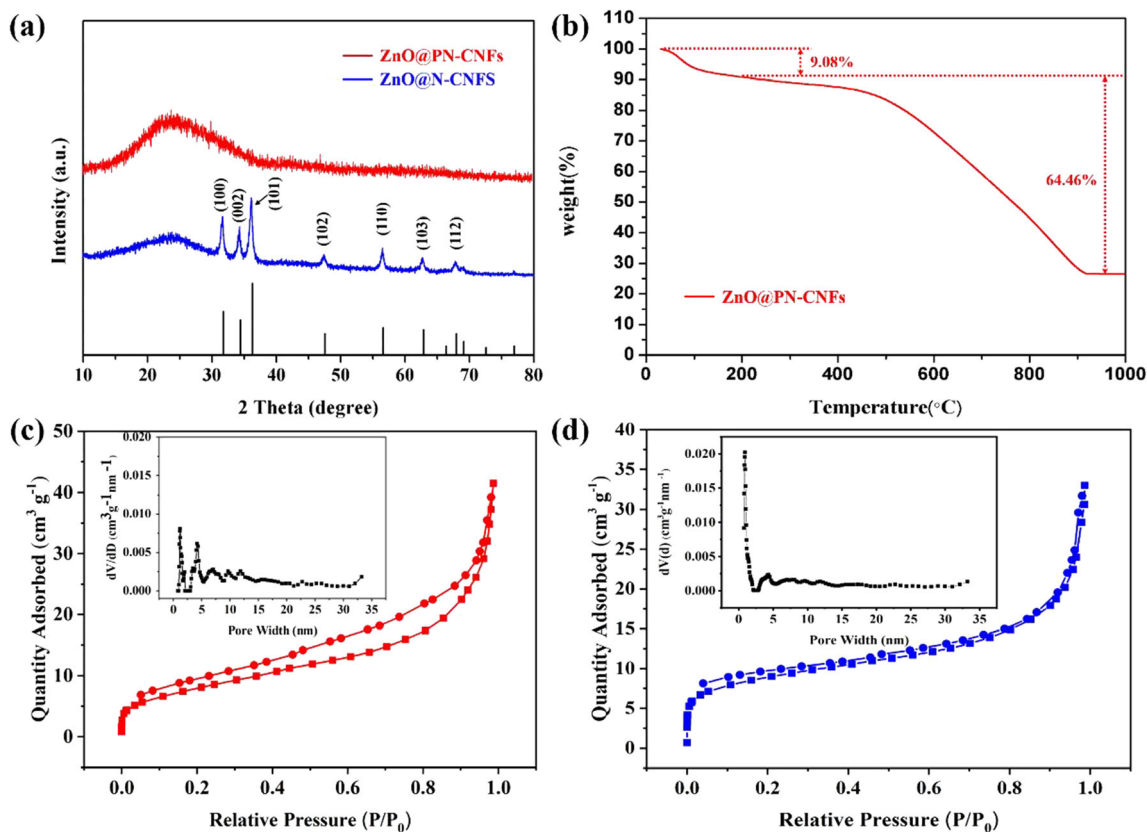


Fig. 4 **a** XRD patterns of ZnO@PN-CNFs and ZnO@N-CNFs. **b** TG analysis of ZnO@PN-CNFs. **c, d** N₂ isotherms and pore size distribution ZnO@PN-CNFs and ZnO@N-CNFs

stabilization and carbonization in making difference for nanofiber structure; the mesopores were increased and micropores were decreased. The presence of mesopores is beneficial for the transmission of Li ions [45]. Proper pore size can shorten the transport pathway, increase the transport rate of lithium ions, and mitigate the volume change of ZnO during the processes of lithiation and delithiation [44, 46, 47].

Figure 5 a displays the Raman spectra of ZnO@PN-CNFs and ZnO@N-CNFs; two dominant peaks located at 1327 cm⁻¹ and 1575 cm⁻¹ were related to D-band and G-band, respectively [3, 48]. The D-band was assigned to disordered (sp³), while G-band was associated with crystalline graphite (sp²). The intensity ratio (I_D/I_G) of ZnO@PN-CNFs and ZnO@N-CNFs is 1.41 and 1.07, respectively. The I_D/I_G represented the carbon of composites with disordered structures [49]. ZnO@PN-CNFs showed a more disordered structure.

To further identify the surface chemical states of ZnO@PN-CNFs, XPS was carried out. As revealed in Fig. 5b, the characteristic peaks in the XPS spectrum indicated the presence of C, N, O, and Zn elements in ZnO@PN-CNFs. As shown in Fig. 5c, there were three characteristic peaks in the C 1s spectrum fitted at 284.1, 284.8, 286.3, and 288.7 eV that corresponded to C–C, C–N, C=N, and C=O bonds, respectively [23, 44, 50, 51]. According to the O 1s spectrum in Fig. 5d, the peaks at 530.9 eV and 533.8 eV were

indicative of the Zn–O bond, and the peak at 532.1 eV corresponded to C–O bond [50, 52, 53]. The high-resolution spectrum of N 1s displayed three characteristic peaks (Fig. 5e). The peak located at 398.4 eV was corresponding to pyridinic N and the peak at 400.0 eV evidenced the presence of the pyrrolic N, while the peak of 400.5 eV corresponded to graphitic N [53, 54]. Pyridinic N and graphitic N were found to be the most highly active sites for the ORR [55]. As shown in Fig. 5f, the Zn 2p spectrum of ZnO@PN-CNFs contained a peak at 1022 eV (Zn 2p_{3/2}) and another peak at 1045.1 eV (Zn 2p_{1/2}) [23, 54].

The electrochemical properties of the ZnO@PN-CNFs and ZnO@N-CNFs were evaluated in coin cells (CR2032). The CV curves of ZnO@PN-CNFs electrode were tested at a sweep rate of 0.2 mV s⁻¹ in Fig. 6a. In the initial cathodic process, the well-defined peak at around 0.76 V, which is ascribed to the conversion reaction of ZnO to Zn and Li₂O, and the formation of a solid-electrolyte interface (SEI) film due to electrolyte decomposition [30, 56]. The weak peak located at 0.26 V resulted from the alloying reaction of the Zn–Li alloy [23]. The peak near 0 V corresponded to the Li⁺ intercalate reaction into carbon [10]. In the anodic process, the peaks appear at 0.53, 0.8, 1.76, and 2.1 V. The peaks at 0.53 and 0.8 V are corresponding to the multistep dealloying reaction of the Zn–Li alloy [56, 57]. The peaks appearing at 1.76 V

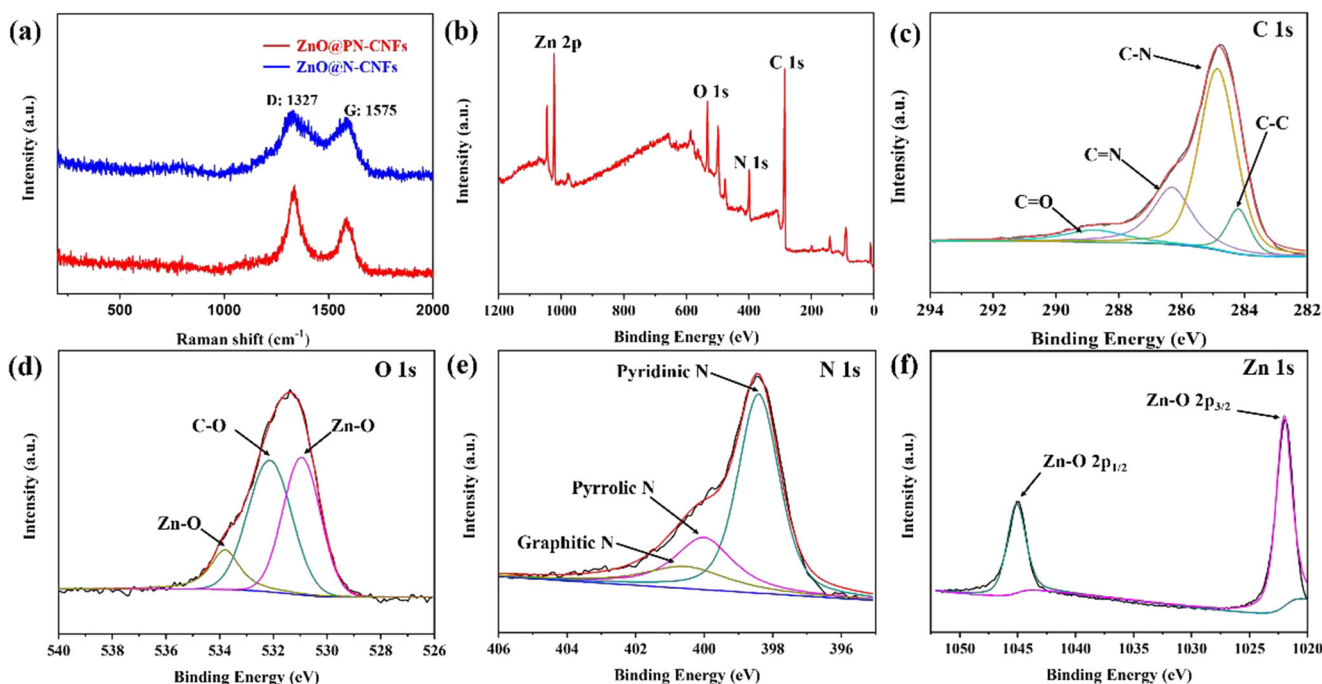


Fig. 5 a Raman spectra of ZnO@PN-CNFs and ZnO@N-CNFs. XPS spectrum of ZnO@PN-CNFs: **b** survey, **c** C 1s, **d** O 1s, **e** N 1s, **f** Zn 2p

and 2.1 V corresponded to the regeneration ZnO (the reaction of Zn and Li_2O) [9, 58]. After one cycle, the CV curve almost overlaps without significant change, indicating the ZnO@PN-CNF electrode possesses excellent reversibility. The electrochemical reactions can be described as follows [23]:

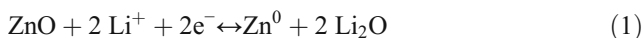


Figure 6 b displays the charge/discharge profiles during 1st, 2nd, 5th, 50th, and 100th cycles at 0.1 A^{-1} . It can be observed that there is a long slope region below the 1V voltage in the initial cycle, which is attributed to the conversion reaction of ZnO, the generation of SEI film, and the alloying reaction of Zn-Li alloy. The initial discharge and charge capacities of the ZnO@PN-CNF electrode are 1836 mAh g^{-1} and $1448.1 \text{ mAh g}^{-1}$, respectively. The capacity loss of 397.1 mAh g^{-1} in first cycle is ascribed to the irreversible loss of electrolyte and the generation of SEI film [27, 28].

Figure 6 c shows the cycling properties of the ZnO@PN-CNF and ZnO@N-CNF electrodes at 0.1 A^{-1} . The ZnO@PN-CNF electrode exhibits higher initial charge and discharge capacity than the ZnO@N-CNF electrode. The initial coulombic efficiency of the ZnO@PN-CNF electrode is 78.87% and quickly stabilizes above 98% after the third cycle, indicating its excellent cycle stability. In the 100th cycle, the discharge capacities of the ZnO@PN-CNF and ZnO@N-CNF electrode

maintain at $1073.2 \text{ mAh g}^{-1}$ and 816.3 mAh g^{-1} , respectively. The capacity of ZnO@PN-CNF electrode is higher than that of ZnO@N-CNF electrode, which is attributed to amorphous ZnO and the special structure. The amorphous phase has more Li ions storage sites than Crystal phase. Moreover, amorphous ZnO particles that disperse uniformly in carbon nanofibers can provide more interface, which can lead to additional capacity.

The rate performance of the ZnO@PN-CNF and ZnO@N-CNF electrodes was tested in the range of 0.1 to 3 A^{-1} every 10 cycles, as shown in Fig. 6d. The reversible discharge capacities of ZnO@PN-CNFs are 1047, 955, 804.3, 653.7, 485.6, and 374.2 mAh g^{-1} at 0.1, 0.2, 0.5, 1, 2, and 3 A^{-1} , respectively. Upon returning the current density to 0.1 A^{-1} , the reversible discharge capacity maintains $1029.2 \text{ mAh g}^{-1}$ while that of ZnO@CNFs electrode is 722 mAh g^{-1} , which indicates that the ZnO@PN-CNF electrode has a higher stability and more excellent reversibility. The mesoporous structure increases the contact area between electrolyte and the ZnO@PN-CNF electrode, resulting in increased transport rate of lithium ions and therefore enhances the electrochemical performance.

Figure 6 e displays the cycling characteristics of the ZnO@PN-CNF and ZnO@N-CNF electrodes at 1 A^{-1} . After 400 cycles, the ZnO@PN-CNF electrode delivers a reversible capacity of 703.1 mAh g^{-1} , and its coulombic efficiency is nearly 100%. The discharge capacity of the ZnO@N-CNF electrode only maintains at 550.4 mAh g^{-1} . At first 200 cycles, the ZnO@N-CNF electrode has a capacity increase process. This phenomenon is due to the amorphization process during the charge and discharge could provide more interface between ZnO and carbon, resulting in

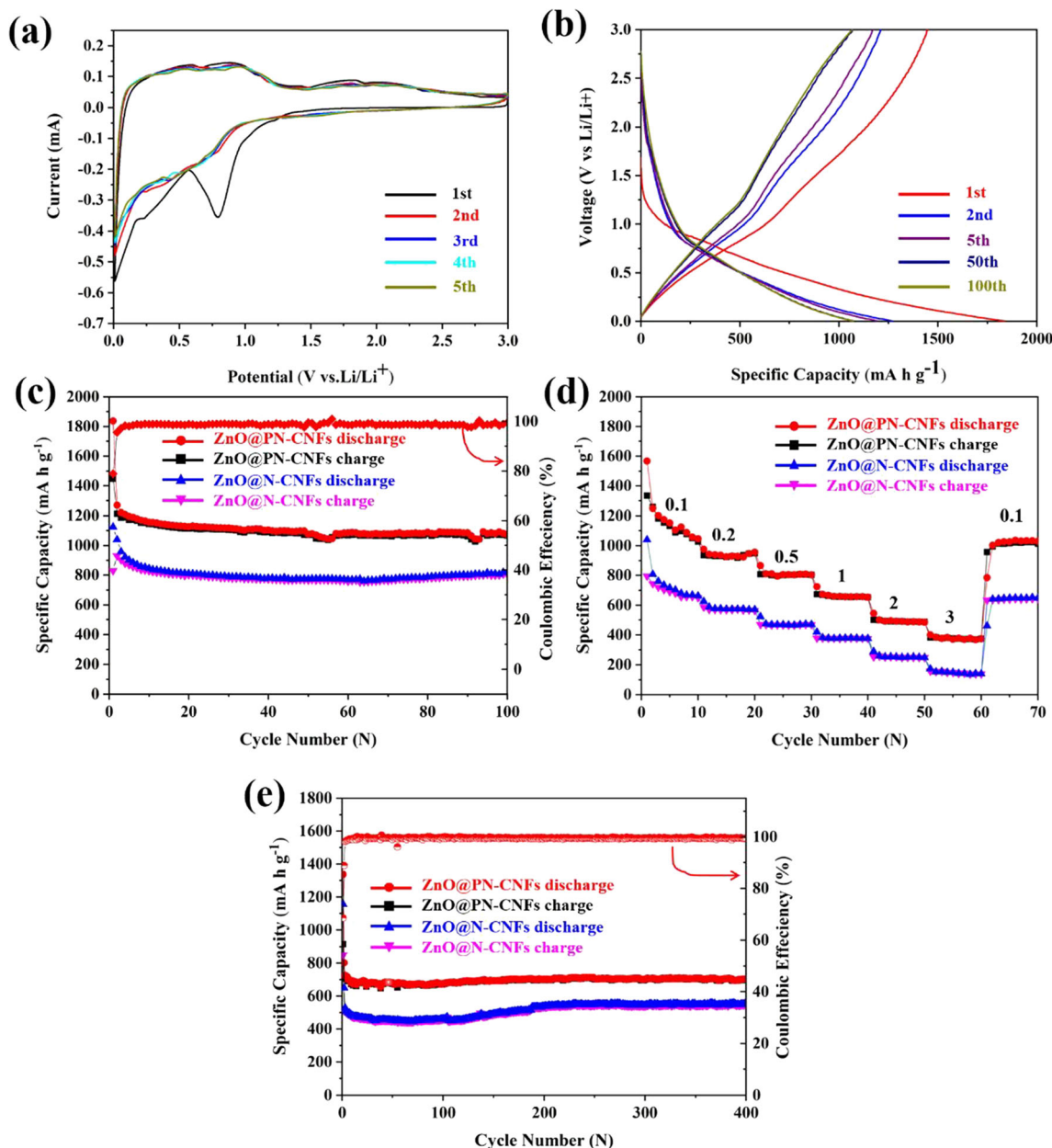


Fig. 6 **a** CV curves of the ZnO@PN-CNFs electrode at a scan rate of 0.2 mV s⁻¹. **b** Discharge/charge profiles of the ZnO@PN-CNFs electrode at a current density of 0.1 A g⁻¹. **c** Cycling performance of the ZnO@PN-

CNFs and ZnO@N-CNFs electrode at 0.1 A g⁻¹. **d** Rate capability of the ZnO@PN-CNFs and ZnO@N-CNFs electrode. **e** Cycling performance of the ZnO@PN-CNFs and ZnO@N-CNFs electrode at 1 A g⁻¹

increased capacity. As for ZnO@PN-CNF electrode, there is no capacity increase process, because amorphous ZnO in the electrode could maintain amorphous state even after many cycles, which will not bring more interface. Moreover, the flat and straight cycling curve of ZnO@PN-CNF electrode in Fig. 6e indicates that the ZnO@PN-CNF electrode has an outstanding cyclic stability and excellent reversibility. Uniformly distributed amorphous ZnO effectively alleviates the volume expansion and avoids pulverization effect, giving the ZnO@PN-CNF electrode more excellent cyclic stability compared to ZnO@N-CNF electrode.

To analyze the reaction kinetics of ZnO@PN-CNF electrode, the CV curves in a scan range of 0.2–1 mV s⁻¹ were conducted (Fig. 7a). The relation of the peak current (*i*) to the scan rate (*v*) is shown in the following formulas [59]:

$$I = a v^b \tag{4}$$

$$\log(i) = b \log(v) + \log(a) \tag{5}$$

Here, *a* is a variable, and *b* value is a parameter calculated from the linear relation between log(*i*) and log(*v*). The

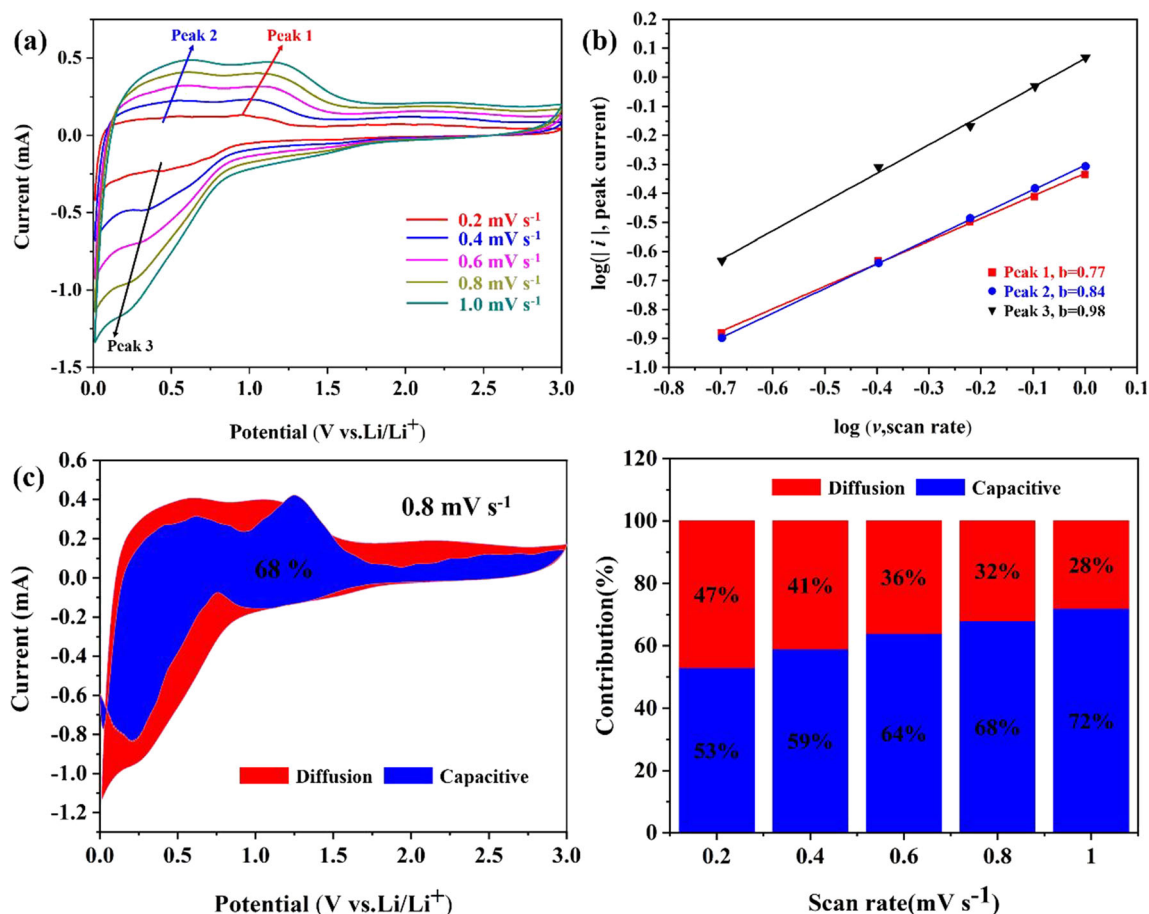


Fig. 7 a CV curves of the ZnO@PN-CNFs electrode at different scan rates. **b** Corresponding $\log(i)$ versus $\log(v)$ plots at each redox peak (peak current: i , scan rate: v) of the ZnO@PN-CNFs electrode. **c** Capacitance

calculated results of three peaks are shown in Fig. 7b. Generally, if $b = 0.5$, electrochemical storage process is diffusion-controlled process, while $b = 1$ is capacitance-controlled process [60]. The b -values of peaks 1, 2, and 3 are 0.777, 0.848, and 0.988, respectively. The b -values of all peaks are close to 1, indicating the coexistence of the capacitance and the diffusion processes [61, 62].

According to the following formula, the contribution of capacitance to the ZnO@PN-CNF electrode can be determined [53]:

$$i = k_1 v + k_2 v^{1/2} \quad (6)$$

In Eq. (5), the relationship can be separated into $k_1 v$ and $k_2 v^{1/2}$, where $k_1 v$ is corresponding to capacitive effect and $k_2 v^{1/2}$ is corresponding to diffusion-controlled effect. Figure 7c shows that the contribution ratio of the capacitance effect is around 68% for the total charge storage at the scan rate of 0.8 mV s^{-1} . Figure 7d indicates the contribution value of capacitance and diffusion at different scanning rates (0.2 – 1 mV s^{-1}). As the scan rate gradually increases, the capacitance

contributions at a scan rate of 0.8 mV s^{-1} . **d** Contribution ratio of capacitance and diffusion at different scan rate

contribution value increases progressively. The fast reaction kinetic results in excellent rate performance.

To further investigate the transport kinetics of materials, the electrochemical impedance spectra were measured. Figure S2 shows the equivalent circuit diagram, the Nyquist plots and the corresponding fitting line of ZnO@PN-CNF and ZnO@N-CNF electrode [38, 63]. The electrolyte resistance (R_e) of ZnO@PN-CNF and ZnO@N-CNF electrode is 2.73Ω and 1.38Ω , respectively. The SEI layer resistance (R_f) of ZnO@PN-CNF and ZnO@N-CNF electrode is 76.8Ω and 85.4Ω , respectively. The charge-transfer resistance (R_{ct}) of the ZnO@PN-CNF electrode (55.6Ω) is lower than the ZnO@N-CNF electrode ($R_{ct} = 61 \Omega$), because nitrogen-doping carbon and active sites of amorphous ZnO improve the electronic conductivity of ZnO@PN-CNF electrode.

Unique 1D porous nanostructure is the reason why ZnO@PN-CNFs show an excellent electrochemical performance. The structure shortens the time to reach stability and does not need to undergo the process of cracking and pulverization to form an amorphous state during the reaction of ZnO crystals and Li ions. The transport interfaces of nanoparticles are almost unchanged before and after the reaction under the

coating of carbon. The existence of mesopores leads to further shortening the distance of the insertion and extraction of Li ions, which is conducive to large current charge and discharge. This is why the capacity of ZnO@PN-CNFs is higher than the comparative sample and the reversible performance is excellent.

Conclusion

In summary, the ZnO@PN-CNFs were successfully prepared by facile urea-assisted electrospinning followed by stabilization and carbonization. The addition of urea changes the morphology of the nanofibers, resulting in the formation of amorphous ZnO. The resulting special structure provides good electron and ion transport capabilities and alleviates the volume change of ZnO@PN-CNFs. The ZnO@PN-CNF electrode delivered a superior reversible capacity of 1073.2 mAh g⁻¹ at 0.1 A⁻¹ for 100 cycles. Besides, the ZnO@PN-CNF electrode displayed a discharge capacity of 703.1 mAh g⁻¹ at 1 A⁻¹ after 400 cycles. The synthesis of zinc oxide is facile and scalable and can be used as a reference for the design of superior-performance anode materials for LIBs.

Funding information This work was supported by the National Natural Science Foundation of Hunan Province, China (Grant No. 2018JJ2513) and National Natural Science Foundation of China (U19A2088).

Compliance with ethical standards

Competing interests The authors declare that they have no competing interests.

References

- Li M, Lu J, Chen Z, Amine K (2018) 30 years of lithium-ion batteries. *Advanced materials*:e1800561. <https://doi.org/10.1002/adma.201800561>
- Chu S, Cui Y, Liu N (2016) The path towards sustainable energy. *Nat Mater* 16(1):16–22. <https://doi.org/10.1038/nmat4834>
- Xie Q, Liu P, Zeng D, Xu W, Wang L, Zhu ZZ, Mai L, Peng DL (2018) Dual electrostatic assembly of graphene encapsulated nanosheet-assembled ZnO-Mn-C hollow microspheres as a lithium ion battery anode. *Adv Funct Mater* 28(19):1707433. <https://doi.org/10.1002/adfm.201707433>
- Li H-H, Wu X-L, Zhang L-L, Fan C-Y, Wang H-F, Li X-Y, Sun H-Z, Zhang J-P, Yan Q (2016) Carbon-free porous Zn₂GeO₄ nanofibers as advanced anode materials for high-performance lithium ion batteries. *ACS Appl Mater Interfaces* 8(46):31722–31728. <https://doi.org/10.1021/acsami.6b11503>
- Xu Q, Sun JK, Yu ZL, Yin YX, Xin S, Yu SH, Guo YG (2018) SiO_x encapsulated in graphene bubble film: an ultrastable Li-ion battery anode. *Adv Mater* 30(25):e1707430. <https://doi.org/10.1002/adma.201707430>
- Xie Q, Zeng D, Ma Y, Lin L, Wang L, Peng D-L (2015) Synthesis of ZnO–ZnCo₂O₄ hybrid hollow microspheres with excellent lithium storage properties. *Electrochim Acta* 169:283–290. <https://doi.org/10.1016/j.electacta.2015.04.041>
- Zhang G, Hou S, Zhang H, Zeng W, Yan F, Li CC, Duan H (2015) High-performance and ultra-stable lithium-ion batteries based on MOF-derived ZnO@ZnO quantum dots/C core-shell nanorod arrays on a carbon cloth anode. *Adv Mater* 27(14):2400–2405. <https://doi.org/10.1002/adma.201405222>
- Su L, Gao L, Hou L, Li J, Yang W, Qin X (2018) Nitrogen-doped porous carbon coated on graphene sheets as anode materials for Li-ion batteries. *Ionics* 25(4):1541–1549. <https://doi.org/10.1007/s11581-018-2713-1>
- Li L, Wang L, Zhang M, Huang Q, Chen L, Wu F (2019) High-performance lithium-ion battery anodes based on Mn₃O₄/nitrogen-doped porous carbon hybrid structures. *J Alloys Compd* 775:51–58. <https://doi.org/10.1016/j.jallcom.2018.10.106>
- Fernando JFS, Zhang C, Firestein Konstantin L, Nerkar JY, Golberg DV (2019) ZnO quantum dots anchored in multilayered and flexible amorphous carbon sheets for high performance and stable lithium ion batteries. *J Mater Chem A* 7(14):8460–8471. <https://doi.org/10.1039/c8ta12511b>
- Cao Z, Zuo C (2017) Cr₂O₃/carbon nanosheet composite with enhanced performance for lithium ion batteries. *RSC Adv* 7(64):40243–40248. <https://doi.org/10.1039/c7ra06188a>
- Li Z, Yin Q, Hu W, Zhang J, Guo J, Chen J, Sun T, Du C, Shu J, Yu L, Zhang J (2019) Tin/tin antimonide alloy nanoparticles embedded in electrospun porous carbon fibers as anode materials for lithium-ion batteries. *J Mater Sci* 54(12):9025–9033. <https://doi.org/10.1007/s10853-019-03539-z>
- Yan C, Chen G, Zhou X, Sun J, Lv C (2016) Template-based engineering of carbon-doped Co₃O₄ hollow nanofibers as anode materials for lithium-ion batteries. *Adv Funct Mater* 26(9):1428–1436. <https://doi.org/10.1002/adfm.201504695>
- Yin X, Chen H, Zhi C, Sun W, Lv L-P, Wang Y (2018) Functionalized graphene quantum dot modification of yolk-shell NiO microspheres for superior lithium storage. *Small* 14(22):1800589. <https://doi.org/10.1002/smll.201800589>
- Deng P, Yang J, Li S, Fan T-E, Wu H-H, Mou Y, Huang H, Zhang Q, Peng D-L, Qu B (2019) High initial reversible capacity and long life of ternary SnO₂-Co-carbon nanocomposite anodes for lithium-ion batteries. *Nano-Micro Letters* 11(1). <https://doi.org/10.1007/s40820-019-0246-4>
- Li H, Wei Y, Zhang Y, Zhang C, Wang G, Zhao Y, Yin F, Bakenov Z (2016) In situ sol-gel synthesis of ultrafine ZnO nanocrystals anchored on graphene as anode material for lithium-ion batteries. *Ceram Int* 42(10):12371–12377. <https://doi.org/10.1016/j.ceramint.2016.05.010>
- Cao YQ, Wang SS, Liu C, Wu D, Li AD (2019) Atomic layer deposition of ZnO/TiO₂ nanolaminates as ultra-long life anode material for lithium-ion batteries. *Sci Rep* 9(1):11526. <https://doi.org/10.1038/s41598-019-48088-2>
- Wang L, Gu X, Zhao L, Wang B, Jia C, Xu J, Zhao Y, Zhang J (2019) ZnO@TiO₂ heterostructure arrays/carbon cloth by charge redistribution enhances performance in flexible anode for Li ion batteries. *Electrochim Acta* 295:107–112. <https://doi.org/10.1016/j.electacta.2018.10.146>
- Xie Q, Lin L, Ma Y, Zeng D, Yang J, Huang J, Wang L, Peng D-L (2017) Synthesis of ZnO-Cu-C yolk-shell hybrid microspheres with enhanced electrochemical properties for lithium ion battery anodes. *Electrochim Acta* 226:79–88. <https://doi.org/10.1016/j.electacta.2016.12.187>
- Wu D, Wang Y, Ma N, Cao K, Zhang W, Chen J, Wang D, Gao Z, Xu F, Jiang K (2019) Single-crystal-like ZnO mesoporous spheres derived from metal organic framework delivering high electron mobility for enhanced energy conversion and storage performances. *Electrochim Acta* 305:474–483. <https://doi.org/10.1016/j.electacta.2019.03.077>

21. Zhang Y, Lu Y, Feng S, Liu D, Ma Z, Wang S (2017) On-site evolution of ultrafine ZnO nanoparticles from hollow metal-organic frameworks for advanced lithium ion battery anodes. *J Mater Chem A* 5(43):22512–22518. <https://doi.org/10.1039/c7ta08284c>
22. Ding Y, Sun J, Liu X (2019) Carbon-decorated flower-like ZnO as high-performance anode materials for Li-ion batteries. *Ionics* 25(9):4129–4136. <https://doi.org/10.1007/s11581-019-02981-y>
23. Zhang G, Zhang H, Zhang X, Zeng W, Su Q, Du G, Duan H (2015) Solid-solution-like ZnO/C composites as excellent anode materials for lithium ion batteries. *Electrochim Acta* 186:165–173. <https://doi.org/10.1016/j.electacta.2015.10.133>
24. Wang XL, Han WQ, Chen H, Bai J, Tyson TA, Yu XQ, Wang XJ, Yang XQ (2011) Amorphous hierarchical porous GeO(x) as high-capacity anodes for Li ion batteries with very long cycling life. *J Am Chem Soc* 133(51):20692–20695. <https://doi.org/10.1021/ja208880f>
25. Minseong Ko SC, Sookyung Jeong, Pilgun Oh, and Jaephil Cho Elastic α -silicon nanoparticle backboneed graphene hybrid as a self-compacting anode for high-rate lithium ion batteries. *ACS Nano*
26. Fang Y, Xiao L, Qian J, Ai X, Yang H, Cao Y (2014) Mesoporous amorphous FePO₄ nanospheres as high-performance cathode material for sodium-ion batteries. *Nano Lett* 14(6):3539–3543. <https://doi.org/10.1021/nl501152f>
27. Ma Y, Ma Y, Geiger D, Kaiser U, Zhang H, Kim G-T, Diemant T, Behm RJ, Varzi A, Passerini S (2017) ZnO/ZnFe₂O₄/N-doped C micro-polyhedrons with hierarchical hollow structure as high-performance anodes for lithium-ion batteries. *Nano Energy* 42:341–352. <https://doi.org/10.1016/j.nanoen.2017.11.030>
28. Liu H, Shi L, Li D, Yu J, Zhang H-M, Ullah S, Yang B, Li C, Zhu C, Xu J (2018) Rational design of hierarchical ZnO@carbon nanoflower for high performance lithium ion battery anodes. *J Power Sources* 387:64–71. <https://doi.org/10.1016/j.jpowsour.2018.03.047>
29. Wu L, Wu T, Mao M, Zhang M, Wang T (2016) Electrospinning synthesis of Ni²⁺, Fe³⁺ codoped ultrafine-ZnFe₂O₄/C nanofibers and their properties for lithium ion storage. *Electrochim Acta* 194:357–366. <https://doi.org/10.1016/j.electacta.2016.02.105>
30. Zhao Q, Xie H, Ning H, Liu J, Zhang H, Wang L, Wang X, Zhu Y, Li S, Wu M (2018) Intercalating petroleum asphalt into electrospun ZnO/Carbon nanofibers as enhanced free-standing anode for lithium-ion batteries. *J Alloys Compd* 737:330–336. <https://doi.org/10.1016/j.jallcom.2017.12.091>
31. Zhao Y, Li X, Dong L, Yan B, Shan H, Li D, Sun X (2015) Electrospun SnO₂-ZnO nanofibers with improved electrochemical performance as anode materials for lithium-ion batteries. *Int J Hydrog Energy* 40(41):14338–14344. <https://doi.org/10.1016/j.ijhydene.2015.06.054>
32. Li Z, Zhang J, Shu J, Chen J, Gong C, Guo J, Yu L, Zhang J (2018) Carbon nanofibers with highly dispersed tin and tin antimonide nanoparticles: preparation via electrospinning and application as the anode materials for lithium-ion batteries. *J Power Sources* 381:1–7. <https://doi.org/10.1016/j.jpowsour.2018.02.004>
33. Kushima A, Liu XH, Zhu G, Wang ZL, Huang JY, Li J (2011) Leapfrog cracking and nanoamorphization of ZnO nanowires during in situ electrochemical lithiation. *Nano Lett* 11(11):4535–4541. <https://doi.org/10.1021/nl201376j>
34. Zhang Y, Wang Z, Li Y, Zhao K (2015) Lithiation of ZnO nanowires studied by in-situ transmission electron microscopy and theoretical analysis. *Mech Mater* 91:313–322. <https://doi.org/10.1016/j.mechmat.2015.05.004>
35. Jin S, Li N, Cui H, Wang C (2013) Growth of the vertically aligned graphene@ amorphous GeOx sandwich nanoflakes and excellent Li storage properties. *Nano Energy* 2(6):1128–1136. <https://doi.org/10.1016/j.nanoen.2013.09.008>
36. Tu Z, Yang G, Song H, Wang C (2016) Amorphous ZnO quantum dot/mesoporous carbon bubble composites for a high-performance lithium-ion battery anode. *ACS Appl Mater Interfaces* 9(1):439–446. <https://doi.org/10.1021/acsami.6b13113>
37. Han F, Li WC, Lei C, He B, Oshida K, Lu AH (2014) Selective formation of carbon-coated, metastable amorphous ZnSnO(3) nanocubes containing mesopores for use as high-capacity lithium-ion battery. *Small* 10(13):2637–2644. <https://doi.org/10.1002/sml.201400371>
38. Zhou P, Chen L, Zhang M, Huang Q, Cui C, Li X, Wang L, Li L, Yang C, Li Y (2019) Embedding α -MnSe nanodots in nitrogen-doped electrospinning carbon nanofibers to enhanced storage properties of lithium-ion batteries. *J Alloys Compd* 797:826–833. <https://doi.org/10.1016/j.jallcom.2019.05.107>
39. An GH, Lee DY, Ahn HJ (2017) Tunneled mesoporous carbon nanofibers with embedded ZnO nanoparticles for ultrafast lithium storage. *ACS Appl Mater Interfaces* 9(14):12478–12485. <https://doi.org/10.1021/acsami.7b01286>
40. Chu Y, Guo L, Xi B, Feng Z, Wu F, Lin Y, Liu J, Sun D, Feng J, Qian Y, Xiong S (2018) Embedding MnO@Mn₃O₄ nanoparticles in an N-doped-carbon framework derived from Mn-organic clusters for efficient lithium storage. *Adv Mater* 30(6). <https://doi.org/10.1002/adma.201704244>
41. Wu Q, Liu J, Yuan C, Li Q, Wang H-g (2017) Nitrogen-doped 3D flower-like carbon materials derived from polyimide as high-performance anode materials for lithium-ion batteries. *Appl Surf Sci* 425:1082–1088. <https://doi.org/10.1016/j.apsusc.2017.07.118>
42. Shen X, Mu D, Chen S, Huang R, Wu F (2014) Electrospun composite of ZnO/Cu nanocrystals-implanted carbon fibers as an anode material with high rate capability for lithium ion batteries. *J Mater Chem A* 2(12):4309. <https://doi.org/10.1039/c3ta14685e>
43. Joshi BN, An S, Jo HS, Song KY, Park HG, Hwang S, Al-Deyab SS, Yoon WY, Yoon SS (2016) Flexible, freestanding, and binder-free SnO(x)-ZnO/carbon nanofiber composites for lithium ion battery anodes. *ACS Appl Mater Interfaces* 8(14):9446–9453. <https://doi.org/10.1021/acsami.6b01093>
44. Zhao J, Wen X, Xu H, Wen Y, Lu H, Meng X (2019) Salting-out and salting-in of protein: a novel approach toward fabrication of hierarchical porous carbon for energy storage application. *J Alloys Compd* 788:397–406. <https://doi.org/10.1016/j.jallcom.2019.02.252>
45. Jing M, Li F, Chen M, Long F, Wu T (2019) Binding ZnO nanorods in reduced graphene oxide via facile electrochemical method for Na-ion battery. *Appl Surf Sci* 463:986–993. <https://doi.org/10.1016/j.apsusc.2018.09.038>
46. Su L, Kong L, Hao S, Zhao Y, Ma Z, Qin X, Shao G (2019) Honeycomb-like porous carbon with nanographitic domains, supported on graphene layers: applicability for lithium/sodium storage. *ACS Sustain Chem Eng* 7(12):10986–10994. <https://doi.org/10.1021/acssuschemeng.9b02078>
47. Xu S, Zhang Z, Wu T, Xue Y (2017) Nanoporous carbon microspheres as anode material for enhanced capacity of lithium ion batteries. *Ionics* 24(1):99–109. <https://doi.org/10.1007/s11581-017-2191-x>
48. Lu X, Xie A, Jiang C, Lu M, Zhang Y, Zhong H, Zhuang S (2017) Synthesis of well-dispersed ZnO-Co-C composite hollow microspheres as advanced anode materials for lithium ion batteries. *RSC Adv* 7(8):4269–4277. <https://doi.org/10.1039/c6ra26816a>
49. Weng S-C (2019) Synthesis of self-assembled hollow-sphere ZnO/rGO nanocomposite as anode materials for lithium-ion batteries. *Int J Electrochem Sci* :3727–3739. <https://doi.org/10.20964/2019.04.63>
50. Yan Y, Wang B, Yan C, Kang DJ (2019) Decorating ZnO nanoflakes on carbon cloth: Free-standing, highly stable lithium-ion battery anodes. *Ceram Int* 45(13):15906–15912. <https://doi.org/10.1016/j.ceramint.2019.05.097>

51. Yu K, Wang L, Wang X, Liu W, Liang J, Liang C (2019) Synthesis of zinc-cobalt bimetallic oxide anchored on the surface of rice husk carbon as anode for high-performance lithium ion battery. *J Phys Chem Solids* 135:109112. <https://doi.org/10.1016/j.jpccs.2019.109112>
52. Ullah I, Xu Y, Wu R, Zhang Y, Wang C, Li L (2019) Heterostructure ZnO-MnO network with graphene for improved lithium ions storage anode. *J Alloys Compd* 802:591–599. <https://doi.org/10.1016/j.jallcom.2019.06.112>
53. Zhang Y, Wang Z, Zaman F, Zhao Z, Sun X, Zhang J, Hou L, Yuan C (2019) Hollow mesoporous hetero-ZnO/ZnMnO₃ microspheres: template-free formation process and enhanced lithium storage capability towards Li-ion batteries as a competitive anode. *J Mater Chem A* 7(7):3264–3277. <https://doi.org/10.1039/c8ta10911g>
54. Li R, Yue W, Chen X (2019) Fabrication of porous carbon-coated ZnO nanoparticles on electrochemical exfoliated graphene as an anode material for lithium-ion batteries. *J Alloys Compd* 784:800–806. <https://doi.org/10.1016/j.jallcom.2019.01.117>
55. Yang J, Xu M, Wang J, Jin S, Tan B (2018) A facile approach to prepare multiple heteroatom-doped carbon materials from imine-linked porous organic polymers. *Sci Rep* 8(1):4200. <https://doi.org/10.1038/s41598-018-22507-2>
56. Gao Y, Li J, Lai X, Hou Y, Zhang W, Yue B, Huang X, Li Y (2019) In situ synthesis of ZnO/porous carbon microspheres and their high performance for lithium-ion batteries. *physica status solidi (a)* 216(6):1800719. <https://doi.org/10.1002/pssa.201800719>
57. Kim H, Jae W, Song J, Kim J (2019) Skein-shaped ZnO/N-doped carbon microstructures as a high performance anode material for lithium-ion batteries. *J Alloys Compd* 772:507–515. <https://doi.org/10.1016/j.jallcom.2018.09.198>
58. Chen S (2016) Lithium-ion batteries anodic performance of porous Sn/C-ZnO core-shell structures derived from ZIF-8. *Int J Electrochem Sci* :10522-10535. <https://doi.org/10.20964/2016.12.62>
59. Zhang J, Chu R, Chen Y, Jiang H, Zeng Y, Chen X, Zhang Y, Huang NM, Guo H (2019) MOF-derived transition metal oxide encapsulated in carbon layer as stable lithium ion battery anodes. *J Alloys Compd* 797:83–91. <https://doi.org/10.1016/j.jallcom.2019.04.162>
60. Tang X, Liang M, Zhang Y, Sun W, Wang Y (2019) Ultrafine ternary metal oxide particles with carbon nanotubes: a metal-organic-framework-based approach and superior lithium-storage performance. *Dalton Trans* 48(13):4413–4419. <https://doi.org/10.1039/c8dt05055d>
61. Ma J, Wang X, Wang G, Wang H (2019) Zinc ferrite nanorod-assembled mesoporous microspheres as advanced anode materials for sodium-ion batteries. *Energy Technology* 7(10):1900479. <https://doi.org/10.1002/ente.201900479>
62. Sinha S, Didwal PN, Nandi DK, Verma R, Cho JY, Kim SH, Park CJ, Heo J (2019) Revealing the simultaneous effects of conductivity and amorphous nature of atomic-layer-deposited double-anion-based zinc oxysulfide as superior anodes in Na-ion batteries. *Small* 15(37):e1900595. <https://doi.org/10.1002/sml.201900595>
63. Cui C, Wei Z, Zhou G, Wei W, Ma J, Chen L, Li C (2018) Quasi-reversible conversion reaction of CoSe₂/nitrogen-doped carbon nanofibers towards long-lifetime anode materials for sodium-ion batteries. *J Mater Chem A* 6(16):7088–7098. <https://doi.org/10.1039/c8ta01168k>

Publisher's note Springer Nature remains neutral with regard to jurisdictional claims in published maps and institutional affiliations.